### Machine Learning for Electron-Scale Turbulence Modeling in W7-X

Ionuț-Gabriel Farcaș, <sup>1, a)</sup> Don Lawrence Carl Agapito Fernando, <sup>2, b)</sup> Alejandro Bañón Navarro, <sup>2, c)</sup> Gabriele Merlo, <sup>2, d)</sup> and Frank Jenko<sup>2, e)</sup>

Constructing reduced models for turbulent transport is essential for accelerating profile predictions and enabling manyquery tasks such as uncertainty quantification, parameter scans, and design optimization. This paper presents machinelearning-driven reduced models for Electron Temperature Gradient (ETG) turbulence in the Wendelstein 7-X (W7-X) stellarator. Each model predicts the ETG heat flux as a function of three plasma parameters: the normalized electron temperature radial gradient ( $\omega_{T_e}$ ), the ratio of normalized electron temperature and density radial gradients ( $\eta_e$ ), and the electron-to-ion temperature ratio ( $\tau$ ). We first construct models across seven radial locations using regression and an active machine-learning-based procedure. This process initializes models using low-cardinality sparse-grid training data and then iteratively refines their training sets by selecting the most informative points from a pre-existing simulation database. We evaluate the prediction capabilities of our models using out-of-sample datasets with over 393 points per location, and 95% prediction intervals are estimated via bootstrapping to assess prediction uncertainty. We then investigate the construction of generalized reduced models, including a generic, position-independent model, and assess their heat flux prediction capabilities at three additional locations. Our models demonstrate robust performance and predictive accuracy comparable to the original reference simulations, even when applied beyond the training domain.

### I. INTRODUCTION

The scientific landscape is being reshaped by rapid advances in data-driven modeling and machine learning (ML). One field poised to benefit significantly is the study of turbulent transport in magnetic confinement fusion devices – a central challenge in fusion research. Understanding plasma turbulence is a key prerequisite for designing optimized fusion power plants. Although high-fidelity first-principles simulations are essential for uncovering the complex physics involved, their high computational cost limits their use for rapid profile predictions and many-query tasks, such as uncertainty quantification, parameter scans, and design optimization, which usually require large ensembles of expensive simulations. These applications demand reduced models with high computational efficiency and predictive reliability.

This paper focuses on the efficient construction of robust reduced models for electron temperature gradient (ETG) turbulence in the Wendelstein 7-X (W7-X) stellarator. For over two decades, ETG turbulence has been a significant subject of theoretical and numerical investigation. Early seminal works<sup>1-3</sup> primarily focused on tokamak core plasmas, whereas more recent studies have increasingly indicated its role in regulating transport within the tokamak pedestal region<sup>4-17</sup> and in stellarators<sup>18-20</sup>. Recognizing this importance, several recent studies<sup>10,21-24</sup> developed reduced models to describe ETG heat fluxes in the tokamak pedestal. For instance, Hatch *et al.* <sup>22</sup> derived simple algebraic formulae for the electron heat flux using a database of 61 discharges

from JET, DIII-D, ASDEX Upgrade, and C-MOD experiments. These formulae were further developed and extended to scaling laws by Hatch *et al.* <sup>23</sup> using a refined version of this database. In a different approach, Farcaş, Merlo, and Jenko <sup>24</sup> formulated a reduced model as a scaling law using structure-exploiting sparse grids <sup>25</sup> and evaluated its prediction capabilities against within-distribution, out-of-bounds, and out-of-distribution datasets. Separately, other recent work by Turica *et al.* <sup>26</sup> employed turbulence models and ML to predict electron temperature profiles in the JET pedestal region.

While progress has been made on reduced models for ETG transport in tokamaks, their development for stellarators remains largely underexplored; this work addresses this gap by constructing reduced ETG turbulence models for W7-X. Our models are defined by three key plasma parameters: the normalized electron temperature radial gradient ( $\omega_{T_e}$ ), the ratio of normalized electron temperature and density radial gradients ( $\eta_e$ ), and the electron-to-ion temperature ratio ( $\tau$ ).

We use an ML-driven strategy that combines regression and active learning to efficiently construct the reduced models from small but informative datasets. Our process begins by constructing an initial set of models from datasets with 11-12 points generated using a structure-exploiting sparse grid approach<sup>25</sup>. These models are then iteratively refined through an active-learning-based procedure that selects the most informative training data pairs. This procedure is driven by computing a measure of prediction uncertainty of the models at the current step using a test set of candidate input parameter values  $(\omega_{T_e}, \eta_e, \tau)$ . To quantify this uncertainty, we use bootstrapping<sup>27</sup> to compute 95% prediction intervals for the ETG heat flux as well as the mean prediction for all input triplets in the test set. Bootstrapping provides a robust, distribution-free method for computing prediction intervals. This approach accounts for both data variability and model uncertainty without requiring specific assumptions about the underlying data or noise distributions. We select the input triplet from the test set where the prediction interval's percentage deviation from

<sup>&</sup>lt;sup>1)</sup>Department of Mathematics and Division of Computational Modeling and Data Analytics, Academy of Data Science, Virginia Tech, Blacksburg, Virginia 24061<sup>f)</sup>

<sup>&</sup>lt;sup>2)</sup>Max Planck Institute for Plasma Physics, 85748 Garching, Germany<sup>f)</sup>

a)Electronic mail: farcasi@vt.edu

b) Electronic mail: don.fernando@ipp.mpg.de

c)Electronic mail: alejandro.banon.navarro@ipp.mpg.de

d) Electronic mail: gabriele.merlo@ipp.mpg.de

e)Electronic mail: frank.jenko@ipp.mpg.de

f)I. Farcaş and D. Fernando contributed equally to this work

the mean prediction is greatest. Note that this measure is independent of the true or simulated heat flux value. This input triplet and its corresponding heat flux computed using the high-fidelity simulation are then added to the training dataset. This augmented dataset is then used to retrain the models. To prevent this process from stopping prematurely, we also compute the relative error between this newly added heat flux value and the prediction obtained with the model from the previous active learning step. The active-learning-based iterative procedure stops when both the maximum percentage deviation of the prediction interval and this relative error fall below user-prescribed thresholds. We note that active learning had been previously applied to construct reduced models for fusion plasmas (e.g., Refs. 28,29); however, its use in the context of stellarators remains, to our knowledge, unexplored.

The active learning procedure is generally used online, where the heat flux is simulated after the active learning procedure selects the most informative input parameter values. However, here we leverage a pre-existing database of ETG simulations. We use a percentage of the input values in this database as our active learning testing set. Consequently, our procedure identifies the best model, relative to the metrics driving the active learning process, that the available database can support. The database was generated by the application of the integrated GENE-KNOSOS-Tango simulation framework, which self-consistently couples various physics codes to predict steady-state plasma profiles, to four experimental OP1.2b W7-X scenarios. <sup>30</sup> Our work contributes to a growing interest in using data-driven techniques to build reduced turbulence models for stellarators. For example, a recent study by Landreman et al. 31 investigated using multiple ML techniques including convolutional neural networks to develop surrogate models of ion-temperature-gradient turbulent transport from a database of 200,000 adiabatic-electron gyrokinetic runs.

We use this ML-based approach to construct reduced models for seven radial locations across W7-X, for which we need at most 138 training data points. We evaluate the models' generalization capabilities using the remainder of the pre-existing database, which contains over 393 out-of-sample points per radial location. To quantify prediction uncertainty-a critical step for assessing the generalization of data-driven models beyond training—we again compute 95% prediction intervals via bootstrapping. For a more comprehensive evaluation, we extend our investigation beyond the initial seven radial locations. We explore two strategies for constructing generalized models for arbitrary radial positions: coefficient regression using the model coefficients for the seven radial locations and a position-independent reduced model. We test the heat flux prediction capabilities of these models at three additional radial locations: two within the considered radial domain and one position outside of it. Overall, our results show that our reduced models achieve an acceptable level of accuracy beyond their training domain, with a predictive performance comparable to the reference results. To our knowledge, this study is among the first to systematically derive reduced ETG models across multiple radial locations in a stellarator.

The remainder of this paper is organized as follows. Section II describes the target reduced models as scaling laws.

Section III presents the datasets used for reduced model development and numerical validation. Our ML-driven approach for constructing these models for ETG transport in W7-X at seven radial locations is presented in Sec. IV. In Sec. V, we present the models' generalization capabilities on out-of-sample datasets. Section VI presents two strategies for model generalization and their ETG heat flux predictions at three additional radial locations, including one outside the original seven. Section VII concludes the paper.

### II. TARGET REDUCED MODELS FOR ETG TURBULENCE IN W7-X

We target reduced models for ETG turbulence in W7-X as scaling laws of the form,

$$Q_e/Q_{\rm GB} = c_0 \,\omega_{T_e}^{p_1} \,(\eta_e - 1)^{p_2} \,\tau^{p_3} \,, \tag{1}$$

where  $Q_e$  is the electron heat flux (in W/m<sup>-2</sup>) and  $Q_{\rm GB} = n_e T_e^{5/2} m_e^{1/2}/(eB_{\rm ref}a)^2$  is the flux in gyro-Bohm (GB) units. Here,  $B_{\rm ref}$  is the magnetic field strength on-axis (in T),  $n_e$  is the electron density (in  $10^{19}$  m<sup>-3</sup>),  $T_e$  is the electron temperature (in keV),  $m_e$  is the electron mass, and a is the effective minor radius of the magnetic geometry, defined as  $a = \sqrt{\Psi_{\rm LCFS}/\pi B_{\rm ref}}$ . The quantity  $\Psi_{\rm LCFS}$  denotes the toroidal magnetic flux through the last closed flux surface (LCFS). This model depends on four coefficients  $\{c_0, p_1, p_2, p_3\} \in \mathbb{R}^4$ .

The target model (1) relates  $Q_e/Q_{\rm GB}$  to three key parameters for ETG turbulence: the normalized electron temperature radial gradient,  $\omega_{T_e} = -a/T_e \ dT_e/d\rho$ , the ratio of normalized electron temperature and density radial gradients,  $\eta_e = \omega_{T_e}/\omega_{n_e}$ , and the electron-to-ion temperature ratio,  $\tau = Z_{\rm eff} T_e/T_i$ , where  $T_i$  denotes the ion temperature.  $Z_{\rm eff}$  is the effective ion charge retained in the collision operator, which is the linearized Landau–Boltzmann operator in our simulations. Our simulations make use of hydrogen ions and do not account for impurities, leading to  $Z_{\rm eff} = 1$ . The selection of these three input parameters is motivated by various previous studies  $^{1,23,24,32}$ . We also note that the scaling law in Eq. (1) is similar to those considered in Hatch *et al.*  $^{23}$  and Farcaş, Merlo, and Jenko  $^{24}$  in the context of reduced models for ETG turbulence in the tokamak pedestal.

We will first construct reduced models (1) for seven radial locations  $\hat{\rho} = \rho/a \in \{0.2, 0.3, 0.4, 0.5, 0.6, 0.7, 0.8\}$  (Sec. IV). The dimensionless radial coordinate  $\hat{\rho} = \sqrt{\Psi/\Psi_{LCFS}}$  is defined by the ratio between the  $\Psi$  value of a flux surface and that of the LCFS. We will then investigate generalized reduced models, including a  $\hat{\rho}$ -independent generic model, and test their prediction capabilities for three other locations  $\hat{\rho} \in \{0.1, 0.55, 0.75\}$  (Sec. VI).

# III. DATASETS FOR REDUCED MODEL DEVELOPMENT AND NUMERICAL VALIDATION

This section describes the datasets used to construct and numerically validate our reduced models for ETG transport in W7-X across seven radial locations. Section III A presents the low-cardinality sparse grid datasets used to build the initial models. Section III B details the pre-existing database of high-fidelity simulations. A fraction of this database is used for iterative model refinement while the remainder is employed for assessing the models' generalization capabilities. Finally, Sec. III C presents the data for three additional radial locations used to investigate generalized models.

# A. Low-cardinality sparse grid datasets for constructing the initial reduced models

In the first step, we construct initial or base models for each  $\hat{\rho}$  using data from a structure-exploiting sparse grid approach<sup>25</sup>. This method, previously shown to be effective for constructing predictive reduced models for ETG transport in the tokamak pedestal<sup>24</sup>, employs adaptive refinement to generate the necessary input-output data. Specifically, the approach leverages the anisotropy of parameter influence – that is, in general, only a subset of input parameters significantly affects the output, and their interactions are non-uniform. Consequently, it preferentially refines directions associated with the most influential inputs and input interactions. In principle, this sparse grid method could construct the target ETG reduced models without needing active learning, though it would require careful selection of input parameter bounds for each  $\hat{\rho}$  to obtain the corresponding training datasets. However, unlike in Ref. 24, this study benefits from a large, preexisting high-fidelity database (discussed in Sec. III B). Therefore, here we use the sparse grid approach to develop initial reduced models using a small number of adaptive steps for each  $\hat{\rho}$ . These base models are then iteratively refined by selecting the most informative training data points from a subset of the pre-existing database. We provide a justification for using sparse grid data to construct the initial models in Appendix A.

In the simulations used to obtain the sparse grid datasets, the plasma behavior is modeled using six local input parameters,  $\{\beta_e, \lambda_{\mathrm{De}}, \nu_c, \tau, \omega_{n_e}, \omega_{T_e}\}$ , where  $\beta_e = 403 \times 10^{-5} n_e T_e/B_{\mathrm{ref}}^2$  denotes the ratio of plasma pressure to magnetic pressure and  $\lambda_{De} = 0.9859 \times B_{\mathrm{ref}} n_{\mathrm{e}}^{-1/2}$  is the normalized Debye length. The normalized collision frequency is given by  $v_c = 2.3031 \times 10^{-5} a(\ln \Lambda) n_{\mathrm{e}} T_{\mathrm{e}}^{-2}$ , where  $\ln \Lambda$  is the Coulomb logarithm. The specific bounds for the six local plasma parameters are summarized in Table I. We assume a uniform distribution within these bounds, which are held constant across all  $\hat{\rho}$ . In this setup,  $\eta_e$  varies between 1.5 and 50.0.

These adiabatic-ion simulations were performed using the plasma micro-turbulence gyrokinetic simulation code GENE<sup>1</sup> in the flux-tube limit using a box with  $n_{k_x} \times n_{k_y} \times n_z \times n_{v_{\parallel}} \times n_{\mu} = 192 \times 72 \times 96 \times 32 \times 8$  degrees of freedom in the five-dimensional position-velocity space. Key simulation parameters include  $k_{y,min} \rho_e = 0.025$  and  $L_x \simeq 350 \rho_e$ , where  $\rho_e = v_e/\Omega_e$  is the electron gyroradius,  $v_e = \sqrt{T_e/m_e} = v_{th}/\sqrt{2}$  is the electron reference velocity, and  $\Omega_e = eB_{\rm ref}/m_e$ . In velocity space, a box characterized by  $-3 \le v_{\parallel}/v_{th} \le 3$  and  $0 \le \mu T_e/B_{\rm ref} \le 9$  has been used. We conducted several convergence tests, including runs at the extrema of the two gradi-

Input parameter	Lower bound	* *
$\beta_e$	$4.00 \times 10^{-4}$	$5.00 \times 10^{-2}$
$\lambda_{\mathrm{De}}$	0.0	1.73
$\nu_c$	$1.00 \times 10^{-5}$	$1.00 \times 10^{-3}$
τ	0.80	2.50
$\omega_{n_e}$	0.10	1.00
$\omega_{n_e} \ \omega_{T_e}$	1.50	5.00

Table I: Summary of the six local plasma parameters and their uniform bounds. These bounds define the input space for the sparse grid approach used to generate the low-cardinality datasets for the initial reduced models.

$\hat{ ho}$	Refinement steps	$N_{\rm SG}$	$Q_{e,  m min}/Q_{ m GB}$	$Q_{e,\mathrm{max}}/Q_{\mathrm{GB}}$
0.2	4	11	0.73	52.6
0.3	5	12	0.91	63.1
0.4	4	11	0.83	69.5
0.5	4	11	1.10	73.2
0.6	4	11	0.96	78.8
0.7	5	12	0.09	87.4
0.8	5	12	0.11	97.6

Table II: Number of refinement steps, sparse grid cardinality, and minimum/maximum heat flux values obtained using the initial sparse grid approach.

ent parameters, to confirm that the employed GENE grid resolution was sufficient for accurate results.

Table II presents the number of adaptive refinement steps, the cardinality of the resulting sparse grid, denoted by  $N_{\rm SG} \in \mathbb{N}$ , and the minimum and maximum values of the computed heat flux  $Q_e/Q_{\rm GB}$  for all  $\hat{\rho}$ . The adaptive refinement process utilized between four and five steps, resulting in low-cardinality grids comprising between 11 and 12 points.

### B. Database for iterative model refinement and numerical validation at seven radial locations

The high-fidelity data for active-learning-based iterative model refinement and numerical validation were generated using the GENE-KNOSOS-Tango simulation framework. This framework couples GENE, the neoclassical transport code KNOSOS<sup>33,34</sup>, and the one-dimensional transport solver Tango<sup>35,36</sup> to predict the steady-state plasma temperature and density profiles in stellarators. The workflow is summarized in Fig. 1. By comparing the heat and particle fluxes to their respective sources at each iteration, Tango generates new plasma profiles for each successive GENE and KNOSOS simulation. The variations in the plasma profiles depend on how well the heat and particle balances are satisfied. As a rule of thumb, fluxes that overshoot the sources at any position lead to a local flattening of the profile while fluxes that underestimate the sources result in a steepening instead.

The database used in the present paper consists of the ensemble of all steady-state adiabatic-ion flux-tube simulations used by the GENE-KNOSOS-Tango framework<sup>30</sup> to ob-

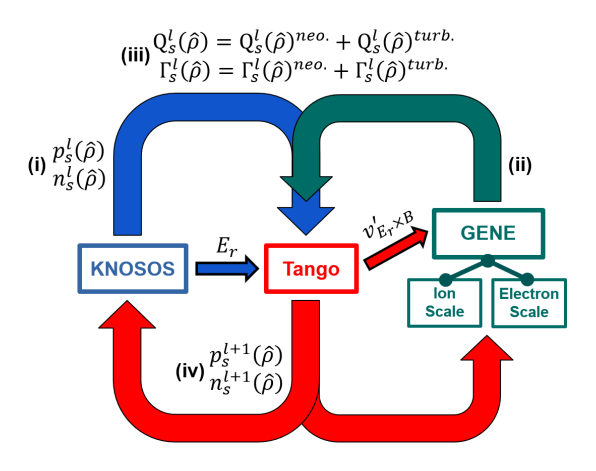


Figure 1: The GENE-KNOSOS-Tango framework evolves the plasma density  $(n_e)$  and pressure  $(p_e, p_i)$  profiles until good agreement between the fluxes and their respective sources (energy or particle) are obtained. A simulation database is created from the input parameters, profiles, and fluxes generated at each iteration l.

tain steady-state temperature and density profiles for four W7-X scenarios, namely the "low-density ECRH", "high-density ECRH", "NBI + ECRH", and "NBI" cases stemming from three OP1.2b experimental campaign discharges. <sup>37,38</sup> Simulations where the electron-scale heat fluxes displayed transient time behavior are excluded from the database. The naming convention reflects the type of heating in these scenarios, which are electron cyclotron resonance heating (ECRH) and neutral-beam injection (NBI). GENE simulations were performed at several radial positions, including those considered in this paper, with the standard magnetic configuration of W7-X while exclusively using the field line passing through the outboard mid-plane of W7-X's bean-shaped cross-section. The target database consists of the electron-scale turbulent heat fluxes  $Q_{\rm e}/Q_{\rm GB}$  and their corresponding input parameters  $\{\omega_{T_e}, \eta_e, \tau\}$  generated using the aforementioned framework. A summary is provided in Table III. The total number of points,  $N_{DB} \in \mathbb{N}$ , ranges from 524 to 967 per position.

#### C. Database for three additional radial locations

For a more comprehensive overview, we will also investigate the construction of generalized models and assess their predictive capabilities at three additional radial locations:  $\hat{\rho} \in \{0.1, 0.55, 0.75\}$ . The data for these three locations were also generated by the Gene-Knosos-Tango framework. The available reference data are summarized in Table IV.

# IV. ACTIVE-LEARNING-BASED ITERATIVE REDUCED MODEL REFINEMENT

To determine the coefficients  $\{c_0, p_1, p_2, p_3\}$  of the target reduced models (1) for each of the seven  $\hat{\rho}$ , we employ

an ML-driven approach that combines regression in logarithmic coordinates, similar to Ref. 24, and iterative refinement based on active learning. For each  $\hat{\rho}$ , we iteratively built the training dataset,  $\mathscr{P}_{\text{train}}$ , consisting input-output pairs  $(\{\omega_{T_e},\eta_e,\tau\},Q_e/Q_{\text{GB}})$ . We denote the cardinality of this dataset by  $N_{\text{train}} \in \mathbb{N}$ . Each iteration progressively enriches  $\mathscr{P}_{\text{train}}$  by adding the most informative input triplet  $\{\omega_{T_e},\eta_e,\tau\}$  and the corresponding heat flux value  $Q_e/Q_{\text{GB}}$ , referred to as the new "label" in an ML context. The specific steps of this procedure are detailed below.

Step I: Training the initial reduced models. We begin by constructing initial or base reduced models (1). For each  $\hat{\rho}$ , the initial training dataset  $\mathscr{P}_{\text{train}}$  solely consists of the  $N_{\text{SG}}$  sparse grid data pairs  $\{(\{\omega_{T_e},\eta_e,\tau\}_i,Q_{e,i}/Q_{\text{GB}})\}_{i=1}^{N_{\text{SG}}}$  from Sec. III A. We then apply regression in logarithmic coordinates using this initial  $\mathscr{P}_{\text{train}}$  to determine the coefficients of the base models for each  $\hat{\rho}$ . The initial models, presented in Eq. 2, show a strong dependence on  $\omega_{T_e}$ , indicated by the large values of  $p_1$  across all radial locations. In contrast, the dependence on  $(\eta_1 - 1)$  and  $\tau$  is less significant.

$$\hat{\rho} = 0.2$$
:  $Q_e/Q_{GB} = 0.35 \,\omega_{T_e}^{3.08} (\eta_e - 1)^{0.41} \tau^{-1.08}$  (2a)

$$\hat{\rho} = 0.3$$
:  $Q_e/Q_{GB} = 0.35 \,\omega_{T_e}^{2.90} (\eta_e - 1)^{0.51} \tau^{-1.08}$  (2b)

$$\hat{\rho} = 0.4$$
:  $Q_e/Q_{GB} = 0.32 \,\omega_{T_e}^{2.99} (\eta_e - 1)^{0.48} \tau^{-0.75}$  (2c)

$$\hat{\rho} = 0.5$$
:  $Q_e/Q_{GB} = 0.45 \, \omega_{T_e}^{2.80} \, (\eta_e - 1)^{0.48} \, \tau^{-0.75}$  (2d)

$$\hat{\rho} = 0.6$$
:  $Q_e/Q_{GB} = 0.10 \,\omega_{T_e}^{3.39} (\eta_e - 1)^{0.78} \tau^{-0.21}$  (2e)

$$\hat{\rho} = 0.7$$
:  $Q_e/Q_{GB} = 0.12 \,\omega_{T_e}^{3.28} (\eta_e - 1)^{0.90} \tau^{-0.25}$  (2f)

$$\hat{\rho} = 0.8: \quad Q_e/Q_{GB} = 0.13 \,\omega_{T_e}^{3.31} \left(\eta_e - 1\right)^{0.79} \tau^{-0.13}$$
 (2g)

Step II: Measuring the models' prediction uncertainty on an input testing set. At each active learning step, we compute a measure of the reduced models' prediction uncertainty using bootstrapping<sup>27</sup>. To do this, we first create test sets of representative input parameter values, Itest, for each radial location. We leverage the pre-existing database summarized in Sec. III B to construct these sets. Specifically, we sort all database entries by their heat flux values in ascending order. Note that this arrangement of entries does not necessarily entail that simulations with similar  $\{\omega_{T_e}, \eta_e, \tau\}$ are closely grouped together.  $\mathscr{I}_{test}$  is then populated with the input triplets  $\{\omega_{T_e}, \eta_e, \tau\}$  from every fourth entry in this sorted list. This yields test sets of size  $|N_{DB}/4|$  for each  $\hat{\rho}$ . The remaining database pairs  $(\{\omega_{T_e}, \eta_e, \tau\}, Q_e/Q_{GB})$ , denoted by  $\mathscr{P}_{pred}$ , are reserved for numerical validation; the corresponding  $N_{\text{pred}} \in \mathbb{N}$  values are listed in the last column in Table V. Our goal with this splitting scheme is to obtain sufficiently representative testing sets while simultaneously reserving large datasets for numerical validation.

Next, we use bootstrapping to create an ensemble of M models for each  $\hat{\rho}$ . Specifically, we resample our current training datasets,  $\mathcal{P}_{\text{train}}$ , with replacement M times to generate M new training datasets of the same size. We then refit our models on each dataset and use them to compute predictions for all input values in  $\mathcal{I}_{\text{test}}$ . This process generates an ensemble of M predictions for each input triplet in the test set,

$\hat{ ho}$	$N_{ m DB}$	$\tau_{min}$	$\tau_{\text{max}}$	$\eta_{e, ext{min}}$	$\eta_{e, ext{max}}$	$\omega_{T_e, \min}$	$\omega_{T_e, \text{max}}$	$Q_{e,  m min}/Q_{ m GB}$	$Q_{e,\mathrm{max}}/Q_{\mathrm{GB}}$
0.2	729	0.93	3.72	1.25	42.14	0.75	3.06	0.02	30.77
0.3	822	0.87	3.40	1.34	32.48	0.47	3.50	0.02	49.06
0.4	674	0.85	2.44	1.62	40.55	0.85	3.75	0.19	80.41
0.5	848	0.84	1.94	1.69	29.51	1.53	3.95	0.46	94.84
0.6	715	0.90	1.62	1.04	17.12	1.55	5.00	0.02	116.71
0.7	524	0.99	1.37	2.03	18.47	1.94	5.15	2.01	136.93
0.8	967	1.01	1.52	1.46	18.00	1.15	13.92	0.70	415.06

Table III: Database for  $\hat{\rho} \in \{0.2, 0.3, 0.4, 0.5, 0.6, 0.7, 0.8\}$  used for iterative model refinement and numerical validation.

ρ	$N_{ m DB}$	$\tau_{min}$	$\tau_{max}$	$\eta_{e, ext{min}}$	$\eta_{e, ext{max}}$	$\omega_{T_e, \min}$	$\omega_{T_e, \text{max}}$	$Q_{e,  m min}/Q_{ m GB}$	$Q_{e,\mathrm{max}}/Q_{\mathrm{GB}}$
0.1	251	0.98	3.85	1.53	17.75	0.58	2.46	0.02	15.97
0.55	70	1.10	1.29	4.79	11.44	1.95	2.63	13.82	41.42
0.75	131	1.02	1.19	2.41	4.06	2.54	5.34	9.52	47.40

Table IV: Database for three addition radial locations  $\hat{\rho} \in \{0.1, 0.55, 0.75\}$  used to test generalized models.

providing an estimate of the prediction distribution and the uncertainty arising from the variability in the training data.

Finally, we use the resulting ensembles to quantify prediction uncertainty. Specifically, we compute the 2.5th and 97.5th percentiles of the predictions from the bootstrap ensemble for each test point, which define the lower and upper bounds of the 95% prediction interval. We also compute the mean of the prediction ensembles. As the size of the training dataset increases, these estimates generally become more accurate and the prediction intervals tend to narrow, providing more reliable uncertainty bounds. While the width of the prediction interval can quantify prediction uncertainty, we instead compute the relative deviation of the interval bounds from the mean prediction. This approach provides a measure of uncertainty that is independent of the wide-ranging magnitude of the heat flux values (from  $\sim$ 0.2 to over 400; see Table III). To ensure a robust estimation of these values, we employ M = 10,000 bootstrap samples in our experiments.

Step III: Active-learning-based model refinement. The active learning procedure selects the input triplet  $\{\omega_{T_e}, \eta_e, \tau\}$ from the test set that has the largest deviation of the prediction interval bounds from the mean prediction. Once selected, this input is removed from  $\mathscr{I}_{\text{test}}$  and is added to the training dataset,  $\mathcal{P}_{train}$ , along with its corresponding heat flux value (or "label" in ML terminology). The models are then retrained on this augmented dataset, completing one cycle. We note that although active learning is typically performed online, where  $\mathcal{I}_{\text{test}}$  might consist, for example, of a large number of pseudorandom samples of inputs, our use of the pre-existing database is a pragmatic choice made to demonstrate the method's efficacy within the constraints of our data. The core of our overall procedure is to efficiently and robustly identify the 'best' models that the available database can support, relative to the guiding active learning metrics.

Step IV: Convergence and final model construction. We repeat Steps II and III until the maximum deviation of the prediction interval bounds from the mean falls below a user-defined tolerance. However, this single criterion may be insufficient because a small deviation does not guarantee that

â	λI	λī
ρ	$N_{\rm train}$	$N_{\text{pred}}$
0.2	84	547
0.3	138	617
0.4	67	506
0.5	73	636
0.6	110	537
0.7	63	393
0.8	91	726

Table V: The cardinality of the training dataset  $(N_{train})$  at the end of the iterative model refinement procedure and the number of validation data pairs  $(N_{pred})$ .

the estimated predictions are close to the true heat flux values. To mitigate this, we introduce a second criterion; we also compute the relative error between the newly added heat flux value and its prediction computed using the model from the previous active learning step. The procedure now terminates when both the maximum deviation and relative error fall below user-prescribed thresholds, denoted by max\_dev > 0 and max\_rel\_err > 0, respectively. Upon termination, the resulting training dataset with cardinality  $N_{\text{train}}$  is used to construct the final reduced model for each  $\hat{\rho}$  via regression in logarithmic coordinates. We note that the values of the two active learning thresholds, max dev and max rel err, can be decreased if necessary throughout the procedure. In our experiments, we used  $max_dev = max_rel_err = 0.15$ . Further decreasing these thresholds results in minimal improvements to the models' accuracy. The final values of  $N_{\text{train}}$  for each  $\hat{\rho}$  are shown in Table V and range between 73 and 138. The corresponding numerical validation sets have between 4 to 8.7 times more points, therefore enabling a comprehensive evaluation of the generalization capabilities of these models.

The obtained reduced models are presented in Eq. (3). First, the signs of the exponents for the model variables reflect their influence on the ETG heat flux. The normalized electron temperature radial gradient  $\omega_{T_e}$  is a primary driver of the instability, which justifies the positive exponent of this term. The parameter  $\eta_e$ , which is the ratio of  $\omega_{T_e}$  to  $\omega_{n_e}$ , captures compet-

ing effects; the temperature gradient destabilizes ETG modes, while the density gradient stabilizes them. Therefore, a positive exponent for  $\eta_e$  is expected. Lastly, increasing the temperature ratio  $\tau$  has a stabilizing effect on ETG modes, leading to a negative exponent for this variable. Considering the radial trend, the exponent of  $\eta_e - 1$  in these models varies little with  $\hat{\rho}$ , indicating a similar dependency on this term radially. The exponent for  $\tau$  (i.e.,  $p_3$ ) generally shows a decreasing trend in absolute value towards the W7-X edge. This is consistent with the observation that  $\tau$  typically exhibits larger variations near the core and smaller variations near the edge. Similarly, the exponent of  $\omega_{T_e}$  follows a decreasing trend with  $\hat{\rho}$ .

$$\hat{\rho} = 0.2: \quad Q_e/Q_{\rm GB} = 0.17 \, \omega_{T_e}^{2.88} \left(\eta_e - 1\right)^{1.08} \tau^{-1.61} \quad (3a)$$

$$\hat{\rho} = 0.3$$
:  $Q_e/Q_{GB} = 0.22 \omega_{T_e}^{2.41} (\eta_e - 1)^{1.26} \tau^{-1.88}$  (3b)

$$\hat{\rho} = 0.4$$
:  $Q_e/Q_{GB} = 0.28 \,\omega_{T_e}^{2.47} (\eta_e - 1)^{1.04} \tau^{-1.14}$  (3c)

$$\hat{\rho} = 0.5$$
:  $Q_e/Q_{\text{GB}} = 0.31 \,\omega_{T_e}^{2.45} (\eta_e - 1)^{1.09} \tau^{-1.25}$  (3d)

$$\hat{\rho} = 0.6$$
:  $Q_e/Q_{GB} = 0.30 \,\omega_{T_e}^{2.37} (\eta_e - 1)^{1.25} \,\tau^{-1.46}$  (3e)

$$\hat{\rho} = 0.7$$
:  $Q_e/Q_{GB} = 0.54 \,\omega_{T_e}^{2.07} (\eta_e - 1)^{1.04} \,\tau^{-1.04}$  (3f)

$$\hat{\rho} = 0.8: \quad Q_e/Q_{GB} = 0.81 \,\omega_{T_e}^{1.56} (\eta_e - 1)^{1.29} \tau^{-1.38}$$
 (3g)

Figure 2 plots the evolution of the reduced model predictions as the size of the training set increases during the model refinement procedure. Specifically, we plot the results for four heat flux values in the validation set (from small to large) for  $\hat{\rho} \in \{0.2, 0.5, 0.8\}$ . We also quantify our models' prediction uncertainty by computing 95% prediction intervals via bootstrapping <sup>24,27</sup>. Initially, the prediction intervals are wide; the extremely large intervals from the first four iterations have been omitted for clarity. As the training data become more informative, the model predictions become more stable and the interval widths decrease.

Finally, we assess the uncertainty of the inferred model coefficients  $\{c_0, p_1, p_2, p_3\}$  in Eq. 3 by computing their 95% confidence intervals using the percentile bootstrapping approach with M = 10,000 samples. This involves retraining the models M times by resampling with replacement the training set obtained at the end of the active learning procedure. The confidence intervals are then determined by computing the 2.5th and 97.5th percentiles of the resulting M parameter ensembles. Table VI presents the computed confidence bounds and also compares the bootstrapped means with their corresponding deterministic values from Eq. 3. The bootstrapped means are generally close to the deterministic values, which suggests a low bias in the regression estimators. Some discrepancies are observed at  $\hat{\rho} = 0.7$ , which is consistent with the smaller database and, thus, training and testing data sizes at this location, as seen in Tables III and V.

### V. PREDICTIONS USING THE PROPOSED MODELS

In this section, we assess the prediction capabilities of the proposed reduced models for  $\hat{\rho} \in \{0.2, 0.3, 0.4, 0.5, 0.6, 0.7, 0.8\}$  beyond training using the numerical validation datasets  $\mathscr{P}_{pred}$  described in

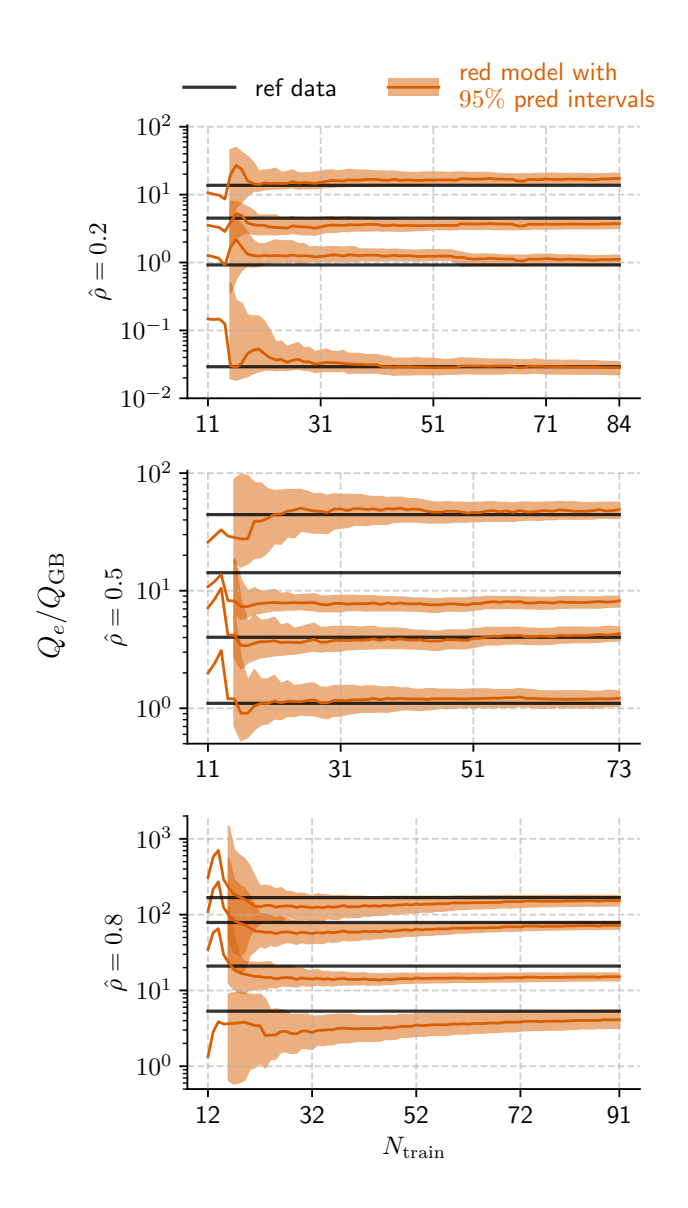


Figure 2: Evolution of reduced model predictions for four heat fluxes from the validation set as a function of  $N_{\text{train}}$  in the active learning procedure for  $\hat{\rho} \in \{0.2, 0.5, 0.8\}$ . The shaded regions represent the 95% prediction intervals computed using bootstrapping. For improved visualization, the very large prediction intervals from the first four iterations have been excluded.

Sec. IV. To evaluate the accuracy of the models' deterministic predictions, we use the error metric from Hatch *et al.* <sup>22,23</sup> and Farcas, Merlo, and Jenko <sup>24</sup>:

$$\varepsilon \left(\frac{Q_{\text{e,ref}}}{Q_{\text{GB}}}, \frac{Q_{\text{e,pred}}}{Q_{\text{GB}}}\right) = \sqrt{\frac{1}{N_{\text{pred}}}} \sum_{i=1}^{N_{\text{pred}}} \frac{\left(Q_{\text{e,ref};i}/Q_{\text{GB}} - Q_{\text{e,pred};i}/Q_{\text{GB}}\right)^{2}}{\left(Q_{\text{e,ref};i}/Q_{\text{GB}} + Q_{\text{e,pred};i}/Q_{\text{GB}}\right)^{2}},$$
(4)

ρ	c <sub>0,CI lo</sub>	C <sub>0,CI</sub> up	$\bar{c}_{0,\mathrm{CI}}$	$c_{0,\mathrm{det}}$	p <sub>1,CI lo</sub>	p <sub>1,CI up</sub>	$\bar{p}_{1,\mathrm{CI}}$	p <sub>1,det</sub>	p <sub>2,CI lo</sub>	P2,CI up	$\bar{p}_{2,\mathrm{CI}}$	p <sub>2,det</sub>	p <sub>3,CI lo</sub>	p <sub>3,CI up</sub>	$\bar{p}_{3,\mathrm{CI}}$	P <sub>3,det</sub>
						3.31										
0.3	0.20	0.25	0.22	0.22	2.23	2.58	2.41	2.41	1.13	1.43	1.26	1.26	-2.17	-1.63	-1.89	-1.89
0.4	0.21	0.34	0.28	0.28	2.19	2.77	2.47	2.47	0.88	1.24	1.04	1.04	-1.61	-0.74	-1.15	-1.14
0.5	0.22	0.39	0.31	0.31	2.13	2.85	2.47	2.45	0.97	1.21	1.09	1.09	-2.03	-0.84	-1.31	-1.25
0.6	0.20	0.44	0.30	0.30	1.96	2.79	2.38	2.37	1.08	1.42	1.25	1.25	-2.30	-0.89	-1.45	-1.46
0.7	0.31	1.21	0.63	0.54	1.55	2.43	2.02	2.07	0.89	1.17	1.03	1.04	-1.69	-0.50	-1.01	-1.04
0.8	0.53	1.26	0.84	0.81	1.35	1.74	1.55	1.56	1.16	1.43	1.29	1.29	-2.30	-0.84	-1.40	-1.34

Table VI: 95% confidence intervals for the inferred model coefficients  $\{c_0, p_1, p_2, p_3\}$ . Intervals are computed using a percentile bootstrapping approach. For each coefficient, the table presents the lower (2.5th percentile) and upper (97.5th percentile) bound and the bootstrapped mean, as well as the point estimate (deterministic value) from the original training dataset.

ρ̂	$arepsilon_{ ext{train}}$	$arepsilon_{ ext{pred}}$	prediction outliers $(\%N_{\text{pred}})$
	0.183		0.025%
0.3	0.195	0.183	0.034%
0.4	0.150	0.159	0.002%
0.5	0.158	0.173	0.004%
0.6	0.189	0.178	0.007%
0.7	0.144	0.139	0.000%
0.8	0.183	0.115	0.005%

Table VII: Errors for training (second column) and numerical validation (third column). The final column shows the percentage of outliers in the validation dataset, defined as inputs with a prediction relative error exceeding 100%.

which compares the  $N_{\rm pred}$  reference electron heat fluxes from the database,  $Q_{\rm e,ref}/Q_{\rm GB}$ , with their corresponding reduced model predictions,  $Q_{\rm e,pred}/Q_{\rm GB}$ . This error equally penalizes extreme over- and under-prediction, that is,  $Q_{\rm e,pred}\gg Q_{\rm e,ref}$  and  $Q_{\rm e,pred}\ll Q_{\rm e,ref}$ . We note, however, that deterministic predictions are often insufficient for practical applications. Therefore, to provide a more comprehensive understanding of model performance, we also quantify prediction uncertainty by computing 95% prediction intervals using bootstrapping.

Table VII shows the errors for both training ( $\varepsilon_{train}$ , second column) and numerical validation ( $\varepsilon_{pred}$ , third column) for all seven  $\hat{\rho}$ . All  $\varepsilon_{train}$  values are below 0.20, indicating that our iteratively refined reduced models (3) reproduce their training data with reasonable accuracy. The true test, however, is their generalization capability, which we discuss next.

Figures 3–9 plot the predictions from our reduced models across all seven  $\hat{\rho}$ . In each figure, the left subplots compare the  $N_{\text{pred}}$  deterministic predictions (from Eq. (3)) with their corresponding reference values from the pre-existing database while also highlighting the values of  $\varepsilon_{\text{pred}}$ . All models exhibit  $\varepsilon_{\text{pred}}$  values consistently below 0.18. Specifically, these errors range from a minimum of  $\varepsilon_{\text{pred}} \approx 0.115$  for  $\hat{\rho} = 0.8$  to  $\varepsilon_{\text{pred}} = 0.183$  for  $\hat{\rho} = 0.3$ . For context, considering the size of our validation datasets, this performance is superior to the existing results for reduced models for ETG turbulence in tokamak pedestals; for example, Farcaş, Merlo, and Jenko <sup>24</sup> reported a minimum error  $\varepsilon_{\text{pred}} \approx 0.2$  for 40 beyond-training predictions, while Hatch *et al.* <sup>23</sup> achieved  $\varepsilon_{\text{pred}} \approx 0.15$  on their training dataset.

For a more detailed understanding of the prediction results,

we also compute the percentage of outliers. We define an outlier as a prediction where the relative error in the  $Q_{\rm e}/Q_{\rm GB}$  value exceeds 100%. The final column in Table VII shows the percentage of the outliers (relative to  $N_{\rm pred}$ ) for each  $\hat{\rho}$ . Outliers are rare, with a maximum of 0.034% of the validation data at  $\hat{\rho}=0.3$ , and no outliers are observed at  $\hat{\rho}=0.7$ . This shows that our models are overall robust and rarely produce significantly inaccurate predictions.

The right subplots in Figures 3–9 show a subset of 40 randomly chosen predictions and their 95% prediction intervals for easier visualization. These plots reveal that the reference heat flux values generally fall within or close to the prediction intervals. Moreover, the plotted prediction intervals are generally narrow, which indicates that the models' predictions have low variability. These results collectively indicate that our reduced models provide robust predictions with a good level of accuracy for data beyond their training domain.

# VI. MODEL GENERALIZATION AND PREDICTIONS FOR THREE ADDITIONAL RADIAL LOCATIONS

We also investigate the construction of generalized reduced models to compute predictions beyond the original seven radial locations. We explore two distinct approaches.

The first approach is to use the fitted model coefficients from Eq. (3) to derive regression-based formulae for the coefficients in the target scaling law (6) as functions of  $\hat{\rho}$ . Details about the derivation of these models are presented in Appendix B. Evaluating the model coefficient formulae (B1) for the three additional radial positions that we are considering in this paper, i.e.,  $\hat{\rho} \in \{0.1, 0.55, 0.75\}$ , yields:

$$\hat{\rho} = 0.1$$
:  $Q_e/Q_{GB} = 0.26 \,\omega_{T_e}^{2.83} (\eta_e - 1)^{1.07} \,\tau^{-1.48}$  (5a)

$$\hat{\rho} = 0.55$$
:  $Q_e/Q_{GB} = 0.42 \,\omega_{T_e}^{2.36} \,(\eta_e - 1)^{1.19} \,\tau^{-1.31}$  (5b)

$$\hat{\rho} = 0.75$$
:  $Q_e/Q_{\rm GB} = 0.72 \, \omega_{T_e}^{1.82} \, (\eta_e - 1)^{1.25} \, \tau^{-1.23}$ . (5c)

Notice that the coefficients of these models are consistent with those in Eq (3) for the original seven radial locations.

The second approach constructs a generic model (6) in which the coefficients are independent of the radial location. To this aim, we apply the active learning procedure described in Sec. IV to data across all radial locations. Since the sparse grid bounds are the same across all  $\hat{\rho}$ , the base model is built

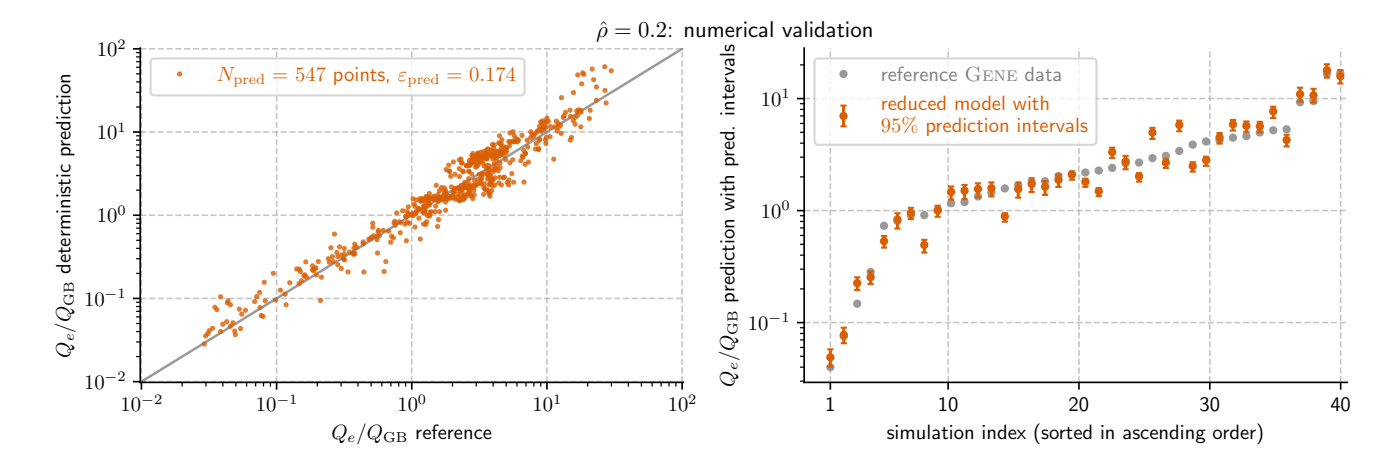


Figure 3: Numerical validation of the reduced model (3a) at  $\hat{\rho} = 0.2$ . The left plot compares its deterministic predictions with all  $N_{\text{pred}} = 547$  reference values. The right plot shows the predictions plus their 95% prediction intervals computed via bootstrapping for a randomly selected subset of 40 points for an easier visualization.

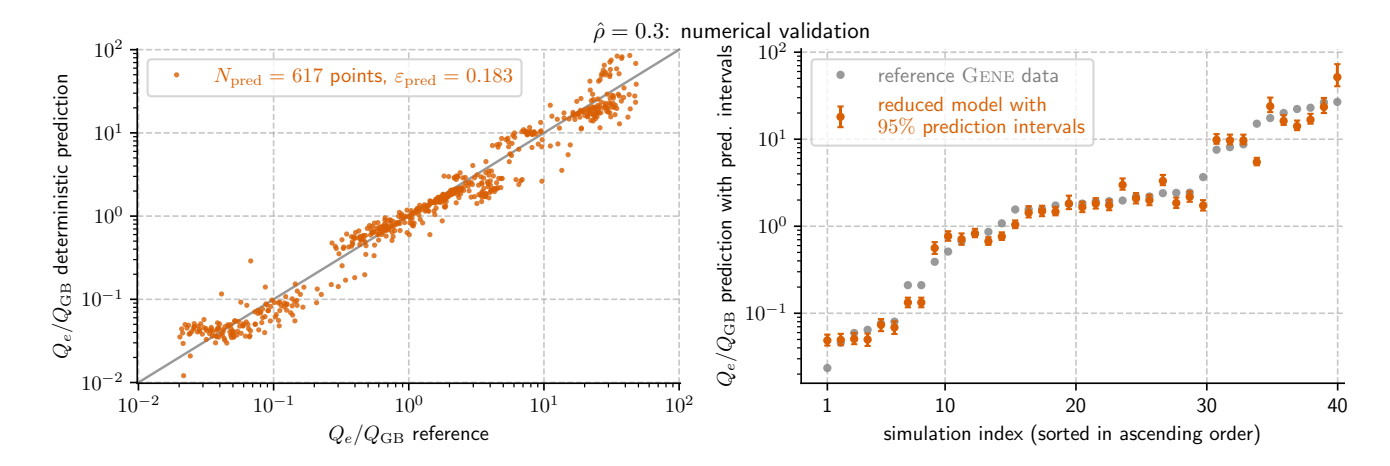


Figure 4: Numerical validation of the reduced model (3b) at  $\hat{\rho} = 0.3$ . The left plot compares its deterministic predictions with all  $N_{\text{pred}} = 617$  reference values. The right plot shows the predictions plus their 95% prediction intervals computed via bootstrapping for a randomly selected subset of 40 points for an easier visualization.

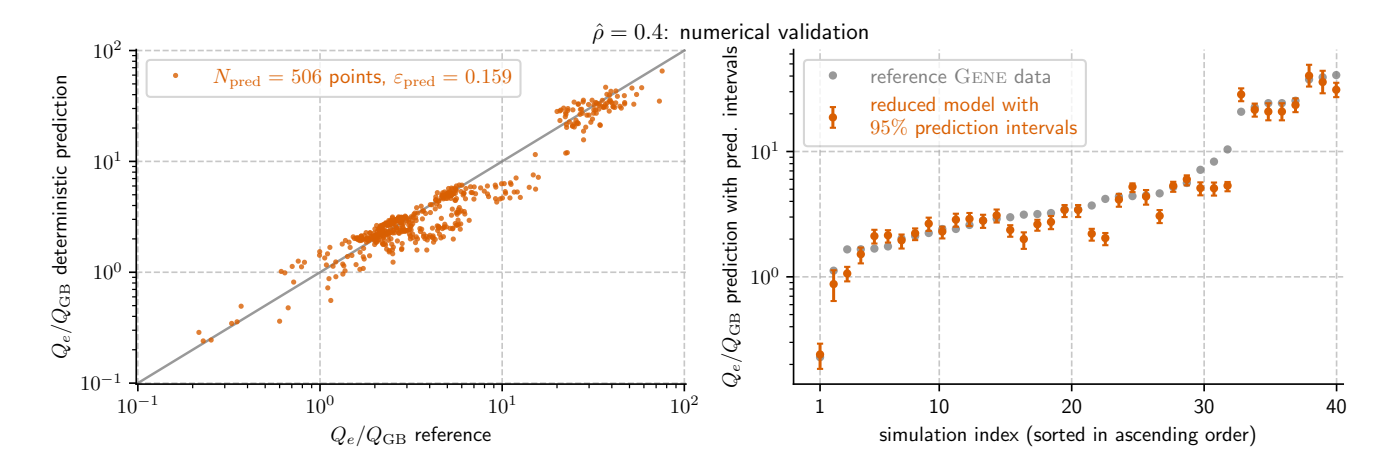


Figure 5: Numerical validation of the reduced model (3c) at  $\hat{\rho} = 0.4$ . The left plot compares its deterministic predictions with all  $N_{\text{pred}} = 506$  reference values. The right plot shows the predictions plus their 95% prediction intervals computed via bootstrapping for a randomly selected subset of 40 points for an easier visualization.

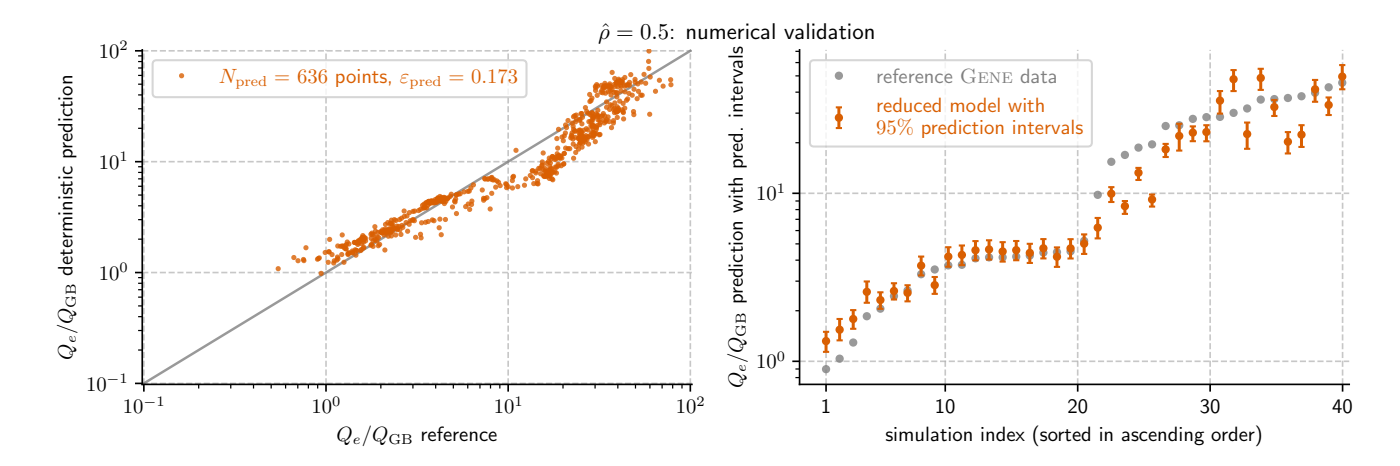


Figure 6: Numerical validation of the reduced model (3d) at  $\hat{\rho} = 0.5$ . The left plot compares its deterministic predictions with all  $N_{\text{pred}} = 636$  reference values. The right plot shows the predictions plus their 95% prediction intervals computed via bootstrapping for a randomly selected subset of 40 points for an easier visualization.

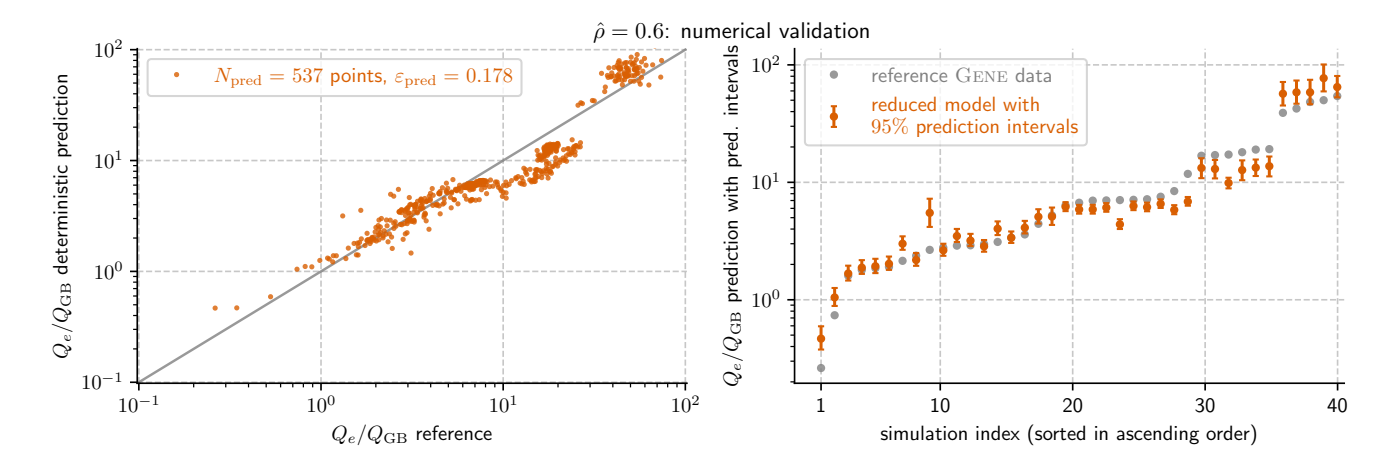


Figure 7: Numerical validation of the reduced model (3e) at  $\hat{\rho} = 0.6$ . The left plot compares its deterministic predictions with all  $N_{\text{pred}} = 537$  reference values. The right plot shows the predictions plus their 95% prediction intervals computed via bootstrapping for a randomly selected subset of 40 points for an easier visualization.

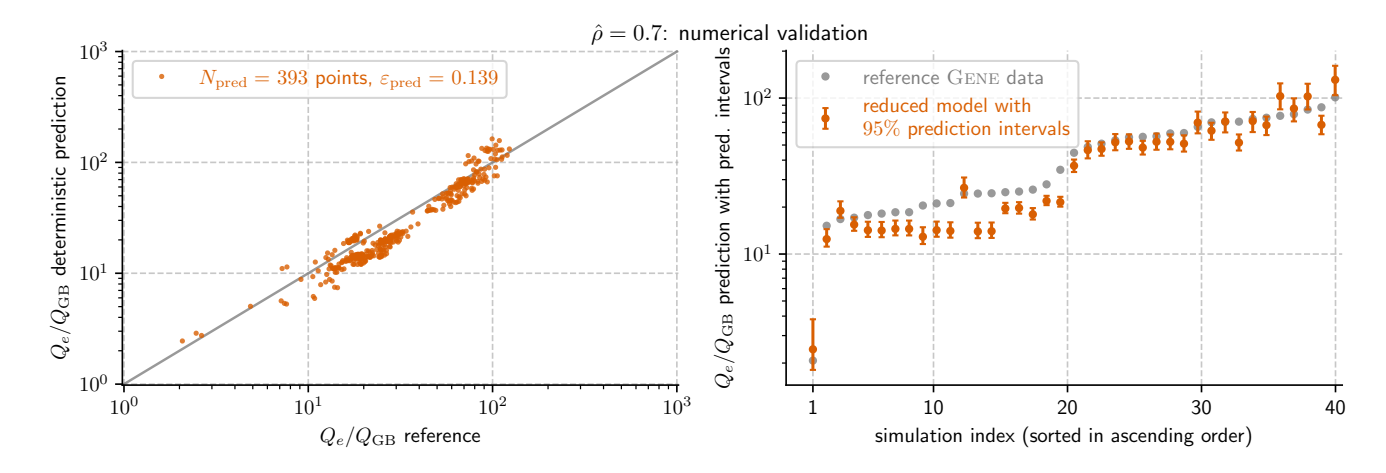


Figure 8: Numerical validation of the reduced model (3f) at  $\hat{\rho} = 0.7$ . The left plot compares its deterministic predictions with all  $N_{\text{pred}} = 393$  reference values. The right plot shows the predictions plus their 95% prediction intervals computed via bootstrapping for a randomly selected subset of 40 points for an easier visualization.

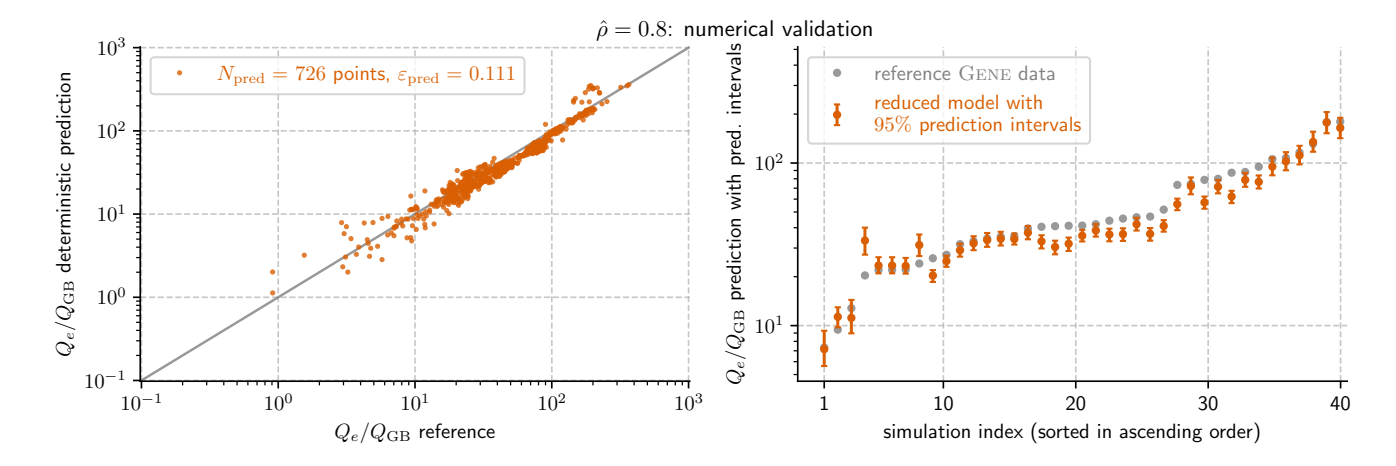


Figure 9: Numerical validation of the reduced model (3g) at  $\hat{\rho} = 0.8$ . The left plot compares its deterministic predictions with all  $N_{\text{pred}} = 726$  reference values. The right plot shows the predictions plus their 95% prediction intervals computed via bootstrapping for a randomly selected subset of 40 points for an easier visualization.

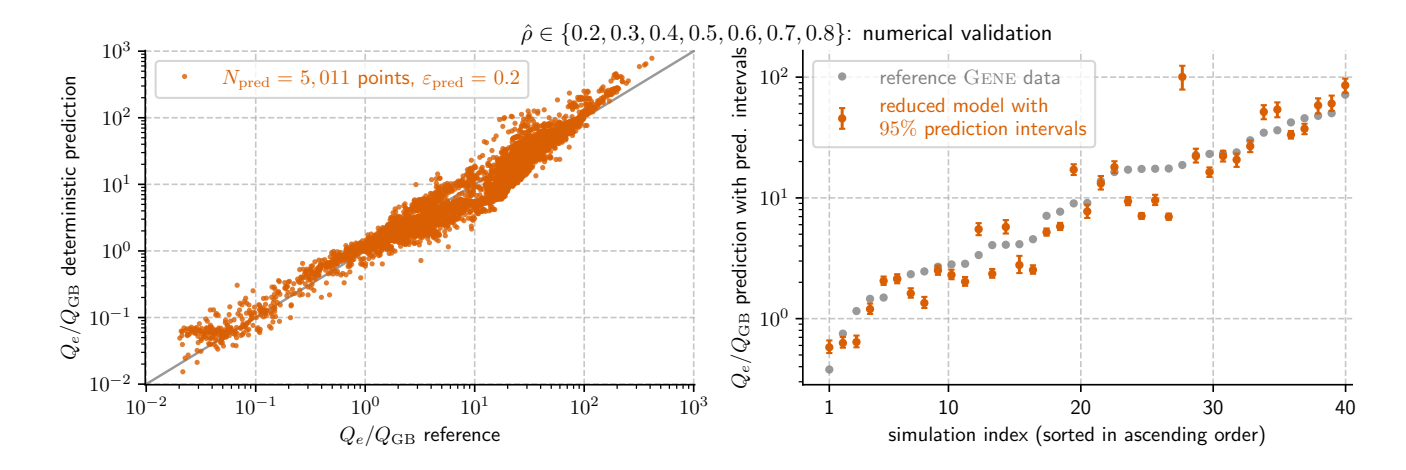


Figure 10: Predictions beyond training using the generic reduced model (6). The left plot compares its deterministic predictions with all  $N_{\text{pred}} = 5,011$  reference values for  $\hat{\rho} \in \{0.2,0.3,0.4,0.5,0.6,0.7,0.8\}$ . The right plot shows the predictions plus their 95% prediction intervals computed via bootstrapping for a randomly selected subset of 40 points for an easier visualization.

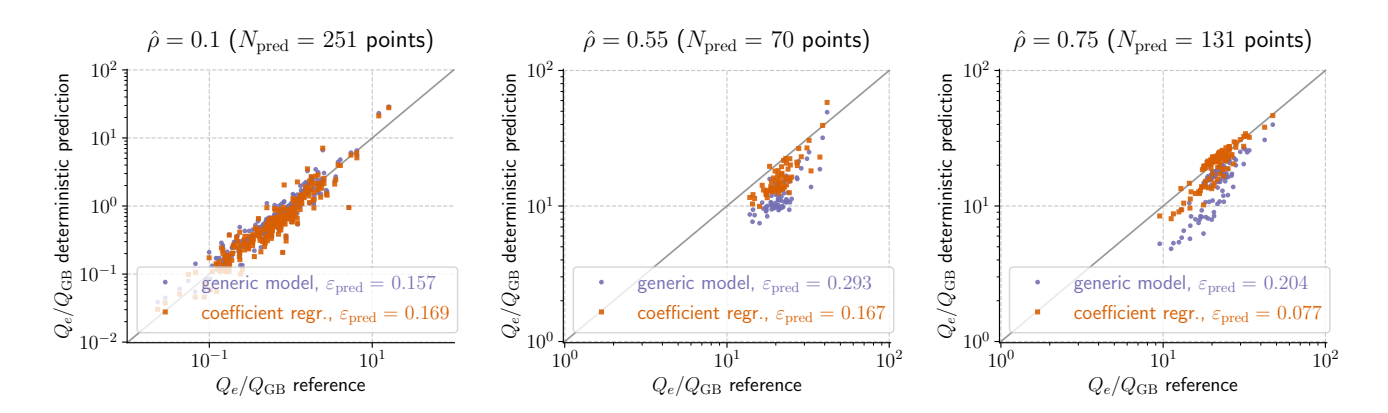


Figure 11: Predictions for  $\hat{\rho} = 0.1$  (left),  $\hat{\rho} = 0.55$  (center), and  $\hat{\rho} = 0.75$  (right) using both the generic model (6) and the three models (5) with coefficients obtained via the regression formulae (B1).

using data from the middle radial location,  $\hat{\rho} = 0.5$ . The testing set for the active learning process is obtained by taking  $\lfloor N_{\rm DB}/20 \rfloor$  of the database inputs for all radial locations. The iterative model refinement procedure stops when max\_dev and max\_rel\_err fall below 10%; this strategy proved most accurate after experimenting with different sizes of the testing set and various values of max\_dev and max\_rel\_err. This yields a training set with  $N_{\rm train} = 225$  data pairs. The resulting model reads:

$$Q_e/Q_{\rm GB} = 0.29 \,\omega_{T_e}^{2.21} (\eta_e - 1)^{1.40} \tau^{-2.23}.$$
 (6)

Its fitted coefficients are comparable to those of the seven individual models, with a slight increase in the exponent of  $(\eta_e - 1)$  and a decrease in the exponent of  $\tau$ . The deterministic training error is  $\varepsilon_{\text{train}} = 0.188$ , which is on par with the training errors of the individual models.

Figure 10 plots the predictions obtained with the generic model (6) against the aggregated validation data across all seven radial locations,  $\hat{\rho} \in \{0.2, 0.3, 0.4, 0.5, 0.6, 0.7, 0.8\}$ . The left plot displays the deterministic predictions for the combined total of  $N_{\text{pred}} = 5,011$  points. The resulting validation error is  $\varepsilon_{\text{pred}} = 0.200$ , which demonstrates a good predictive performance given the overall size and broad parameter space of the validation set. Moreover, the percentage of prediction outliers is 0.024%. The right subplots show the predictions plus their 95% prediction intervals computed via bootstrapping for a randomly selected subset of 40 points for an easier visualization. Here, we observe larger disparities between the reference data and the generic model's predictions compared to the results obtained using the seven individual, position-specific models.

Figure 11 compares the predictions from the generic model (6) against those from the parameter regression models (5) across the three additional radial locations. The generic model performs well at  $\hat{\rho} = 0.1$  and provides reasonable predictions at  $\hat{\rho} = 0.75$ , with deterministic errors ( $\varepsilon_{\text{pred}}$ ) smaller than 0.21. However, it underpredicts the fluxes at  $\hat{\rho} = 0.55$ , resulting in a higher error of 0.293. In contrast, the models based on coefficient regression perform robustly at all three positions. They reduce the errors at  $\hat{\rho} = 0.55$  and  $\hat{\rho} = 0.75$  to approximately 0.169 and 0.077, respectively, while producing minimal outliers. Based on these findings, we can conclude that models with coefficients obtained using the parameter regression formulae (B1) are likely to offer superior predictions. The improved performance is somewhat expected because the regression approach leverages position-specific model coefficients. The resulting coefficients are more representative of the local turbulence characteristics than the single, generic model derived here.

#### VII. SUMMARY AND DISCUSSION

This paper formulated and tested a set of robust machine-learning-based reduced models for electron-temperature-gradient-driven (ETG) turbulence in the Wendelstein 7-X stellarator. Our approach, which combines regression with an iterative active learning process, efficiently constructed mod-

els depending on three key plasma parameters: the normalized electron temperature radial gradient ( $\omega_{T_e}$ ), the ratio of normalized electron temperature and density radial gradients ( $\eta_e$ ), and the electron-to-ion temperature ratio ( $\tau$ ). We also equipped our models with a notion of prediction uncertainty quantification, a step often overlooked in practice but essential for assessing generalization beyond training. Specifically, we computed 95% prediction intervals via bootstrapping. To our knowledge, this study is one of the first to derive and numerically validate such ETG reduced models in a stellarator.

We first built reduced models for seven radial locations  $\hat{\rho} \in$  $\{0.2, 0.3, 0.4, 0.5, 0.6, 0.7, 0.8\}$ , for which the active-learningbased procedure required training sets comprising between 73 and 138 data points. Validation results performed using over 393 out-of-sample points per  $\hat{\rho}$  demonstrated that our models provide robust predictions with an accuracy comparable to the reference high-fidelity results. For a more comprehensive perspective, we also investigated the construction of models for arbitrary radial positions using two approaches. The first was to use the fitted model coefficients for the seven positions to derive regression-based formulae for the coefficients in the target scaling law. The second approach constructed a generic model with fixed coefficients independent of the radial location. Validation efforts at three additional radial locations  $\hat{\rho} \in \{0.1, 0.55, 0.75\}$  showed that the coefficient regression models performed well across all three locations, while the generic model performed well at  $\hat{\rho} = 0.1$ , was reasonable at  $\hat{\rho} = 0.75$ , but underpredicted the fluxes at  $\hat{\rho} = 0.55$ .

Building on the success of the approach presented in this paper, we plan to apply it to ion-scale fluxes as well. Reduced models for the ion-scale electron heat  $(Q_e/Q_{\rm GB})$ , ion heat  $(Q_i/Q_{\rm GB})$ , and particle  $(\Gamma_e/\Gamma_{\rm GB})$  fluxes will be developed and validated in the next step of our research.

### **ACKNOWLEDGMENTS**

I.-G. F. was supported in part by NSF Grant DMS-2436357. This work has been carried out within the framework of the EUROfusion Consortium, funded by the European Union via the Euratom Research and Training Programme (Grant Agreement No 101052200 - EURO-fusion) and by the Spanish Ministry of Science, Innovation and Universities under grant PID2021-125607NB-I00. We acknowledge the EuroHPC Joint Undertaking for awarding access to the EuroHPC supercomputer LUMI, hosted by CSC (Finland) and the LUMI consortium through a EuroHPC Extreme Access call. The simulations were completed under project grant number 465000821. Views and opinions expressed are however those of the author(s) only and do not necessarily reflect those of the European Union or the European Commission. Neither the European Union nor the European Commission can be held responsible for them. Numerical simulations were performed with the Frontera supercomputer at the Texas Advanced Computing Center, USA, the Raven HPC system at the Max Planck Computing and Data Facility, Germany, the Marconi 100 & Leonardo Fusion supercomputer at CINECA, Italy, and the LUMI supercomputer at the CSC data center, Finland.

# Appendix A: Role of sparse grid data in constructing the active learning base models

We justify our methodological choice of using sparse grid data to fit the initial models in the active-learning-based model refinement process. The alternative approach would be to use a subset of the available database for initial fitting. However, the effectiveness of this alternative approach is influenced by the richness and representativeness of the database. To demonstrate this, let us focus on the reduced model at  $\hat{\rho} = 0.7$ . We have performed extensive experiments in which, instead of using the sparse grid data to construct the initial models, we used subsets of 12 (i.e., the same number of points as in the sparse grid dataset) or 30 points from the database. Performing the active learning procedure 10 times where we pseudo-randomly select 12 training points to train the initial model yields the following values for  $c_0, p_1, p_2, p_3$  and  $\varepsilon_{\text{pred}}$ :

$$\begin{array}{c} 1.\ c_0 = 1.10, p_1 = 1.59, p_2 = 0.91, p_3 = 0.23, \varepsilon_{\mathrm{pred}} = 0.105 \\ 2.\ c_0 = 1.14, p_1 = 1.52, p_2 = 0.96, p_3 = 0.18, \varepsilon_{\mathrm{pred}} = 0.105 \\ 3.\ c_0 = 1.06, p_1 = 1.59, p_2 = 0.91, p_3 = 0.19, \varepsilon_{\mathrm{pred}} = 0.118 \\ 4.\ c_0 = 1.01, p_1 = 1.67, p_2 = 0.93, p_3 = -0.24, \varepsilon_{\mathrm{pred}} = 0.107 \\ 5.\ c_0 = 1.00, p_1 = 1.67, p_2 = 0.90, p_3 = 0.43, \varepsilon_{\mathrm{pred}} = 0.104 \\ 6.\ c_0 = 1.11, p_1 = 1.55, p_2 = 0.91, p_3 = 0.34, \varepsilon_{\mathrm{pred}} = 0.115 \\ 7.\ c_0 = 1.00, p_1 = 1.67, p_2 = 0.97, p_3 = -0.45, \varepsilon_{\mathrm{pred}} = 0.103 \\ 8.\ c_0 = 1.01, p_1 = 1.65, p_2 = 0.97, p_3 = -0.41, \varepsilon_{\mathrm{pred}} = 0.105 \\ 9.\ c_0 = 1.00, p_1 = 1.67, p_2 = 0.94, p_3 = -0.27, \varepsilon_{\mathrm{pred}} = 0.105 \\ 10.\ c_0 = 1.12, p_1 = 1.60, p_2 = 0.93, p_3 = -0.14, \varepsilon_{\mathrm{pred}} = 0.100 \end{array}$$

The validation accuracy is comparable to, or even slightly better than, that of the fitted model 3f. Moreover, the values of  $c_0, p_1$ , and  $p_2$  do not vary significantly across the 10 experiments. However,  $p_3$  varies more drastically. The fitted values are inconsistent with those obtained at other radial locations, including physically implausible positive values. Increasing the size of the initial model training dataset to 30 did not resolve the issue. On average, these ten new models show that the ETG heat flux has a very weak dependency on  $\tau$  at  $\hat{\rho} = 0.7$  in the database. A  $p_3$  value consistent with those for the other radial locations (i.e.,  $p_3 \sim -1$ ) was only achieved when the sparse grid data was included in the testing set during the active learning procedure, which is equivalent to our original approach. We attribute this to the narrower range of the parameter  $\tau$  in that specific database subset (see Table III). In contrast, the sparse grid dataset used  $\tau$  values between 0.80 and 2.50. The additional sparse grid data provided new information that is not available in the database. Thus, this wider range was sufficient to yield a fit for  $p_3$  that is consistent with the results obtained at all other radial locations.

### Appendix B: Regression formulae for the scaling law coefficients

The values of the fitted model coefficients in Eq. (3) suggest nonlinear trends for  $c_0$  and  $p_1$  and linear trends for  $p_2$  and  $p_3$ 

with respect to the radial location,  $\hat{\rho}$ . To create robust coefficient regression models and to decrease the chance of overfitting, we selected the following functional forms: quadratic polynomials for  $c_0$  and  $p_1$  and linear functions for  $p_2$  and  $p_3$ . These choices are purely for mathematical convenience and are not intended to imply any physical meaning. To further increase the robustness of our estimates, we eliminate outliers from the curve-fitting procedure. We obtain the following expression for the four model coefficients:

$$c_0(\hat{\rho}) = 1.79\,\hat{\rho}^2 - 0.81\,\hat{\rho} + 0.32$$
 (B1a)

$$p_1(\hat{\rho}) = -2.52\,\hat{\rho}^2 + 0.58\,\hat{\rho} + 2.80$$
 (B1b)

$$p_2(\hat{\rho}) = 0.29\,\hat{\rho} + 1.04$$
 (B1c)

$$p_3(\hat{\rho}) = 0.39\,\hat{\rho} - 1.52.$$
 (B1d)

#### **REFERENCES**

<sup>1</sup>F. Jenko, W. Dorland, M. Kotschenreuther, and B. N. Rogers, Physics of Plasmas 7, 1904 (2000).

<sup>2</sup>W. Dorland, F. Jenko, M. Kotschenreuther, and B. N. Rogers, Physical Review Letters 85, 5579 (2000).

<sup>3</sup>F. Jenko and W. Dorland, Physical Review Letters **89**, 225001 (2002).

<sup>4</sup>D. Told, F. Jenko, P. Xanthopoulos, L. D. Horton, E. Wolfrum, and A. U. Team, Physics of Plasmas **15**, 102306 (2008).

<sup>5</sup>F. Jenko, D. Told, P. Xanthopoulos, F. Merz, and L. D. Horton, Physics of Plasmas **16**, 055901 (2009).

<sup>6</sup>Y. Idomura, Physics of Plasmas **13**, 080701 (2006).

<sup>7</sup>D. Hatch, D. Told, F. Jenko, H. Doerk, M. Dunne, E. Wolfrum, E. Viezzer, T. A. U. Team, and M. Pueschel, Nuclear Fusion **55**, 063028 (2015).

<sup>8</sup>D. Hatch, M. Kotschenreuther, S. Mahajan, P. Valanju, and X. Liu, Nuclear Fusion **57**, 036020 (2017).

<sup>9</sup>E. Hassan, D. Hatch, M. Halfmoon, M. Curie, M. Kotchenreuther, S. Mahajan, G. Merlo, R. Groebner, A. Nelson, and A. Diallo, Nuclear Fusion **62**, 026008 (2021).

<sup>10</sup>B. Chapman-Oplopoiou, D. Hatch, A. Field, L. Frassinetti, J. Hillesheim, L. Horvath, C. Maggi, J. Parisi, C. Roach, S. Saarelma, J. Walker, and J. Contributors, Nuclear Fusion 62, 086028 (2022).

<sup>11</sup>P-Y. Li, D. Hatch, B. Chapman-Oplopoiou, S. Saarelma, C. Roach, M. Kotschenreuther, S. Mahajan, G. Merlo, and M. the Team, Nuclear Fusion 64, 016040 (2023).

<sup>12</sup>J. F. Parisi, F. I. Parra, C. M. Roach, C. Giroud, W. Dorland, D. R. Hatch, M. Barnes, J. C. Hillesheim, N. Aiba, J. Ball, P. G. Ivanov, and J. contributors, Nuclear Fusion 60, 126045 (2020).

<sup>13</sup>J. Parisi, F. Parra, C. Roach, M. Hardman, A. Schekochihin, I. Abel, N. Aiba, J. Ball, M. Barnes, B. Chapman-Oplopoiou, D. Dickinson, W. Dorland, C. Giroud, D. Hatch, J. Hillesheim, J. R. Ruiz, S. Saarelma, D. St-Onge, and J. Contributors, Nuclear Fusion 62, 086045 (2022).

<sup>14</sup>K. Stimmel, L. Gil, T. Görler, M. Cavedon, P. David, M. Dunne, R. Dux, R. Fischer, F. Jenko, A. Kallenbach, and et al., Journal of Plasma Physics 88, 905880315 (2022).

<sup>15</sup>L. Leppin, T. Görler, M. Cavedon, M. Dunne, E. Wolfrum, and F. Jenko, Journal of Plasma Physics 89, 905890605 (2023).

<sup>16</sup>E. A. Belli, J. Candy, and I. Sfiligoi, Plasma Physics and Controlled Fusion 65, 024001 (2022).

<sup>17</sup>E. A. Belli, J. Candy, and I. Sfiligoi, Plasma Physics and Controlled Fusion 66, 045019 (2024).

<sup>18</sup>F. Jenko and A. Kendl, New Journal of Physics **4**, 35 (2002).

<sup>19</sup>G. G. Plunk, P. Xanthopoulos, G. M. Weir, S. A. Bozhenkov, A. Dinklage, G. Fuchert, J. Geiger, M. Hirsch, U. Hoefel, M. Jakubowski, A. Langenberg, N. Pablant, E. Pasch, T. Stange, D. Zhang, and t. W7-X Team, Phys. Rev. Lett. 122, 035002 (2019).

<sup>20</sup>G. Weir, P. Xanthopoulos, M. Hirsch, U. Höfel, T. Stange, N. Pablant, O. Grulke, S. Äkäslompolo, J. Alcusón, S. Bozhenkov, M. Beurskens, A. Dinklage, G. Fuchert, J. Geiger, M. Landreman, A. Langenberg, S. Laz-

- erson, N. Marushchenko, E. Pasch, J. Schilling, E. Scott, Y. Turkin, T. Klinger, and W.-X. the Team. Nuclear Fusion **61**, 056001 (2021).
- <sup>21</sup>W. Guttenfelder, R. Groebner, J. Canik, B. Grierson, E. Belli, and J. Candy, Nuclear Fusion 61, 056005 (2021).
- <sup>22</sup>D. R. Hatch, C. Michoski, D. Kuang, B. Chapman-Oplopoiou, M. Curie, M. Halfmoon, E. Hassan, M. Kotschenreuther, S. M. Mahajan, G. Merlo, M. J. Pueschel, J. Walker, and C. D. Stephens, Physics of Plasmas 29, 062501 (2022).
- <sup>23</sup>D. Hatch, M. Kotschenreuther, P.-Y. Li, B. Chapman-Oplopoiou, J. Parisi, S. Mahajan, and R. Groebner, Nuclear Fusion 64, 066007 (2024).
- <sup>24</sup>I.-G. Farcaş, G. Merlo, and F. Jenko, Journal of Plasma Physics 90, 905900510 (2024).
- <sup>25</sup>I.-G. Farcaş, G. Merlo, and F. Jenko, Communications Engineering 1, 43 (2022).
- <sup>26</sup>L. P. Turica, A. R. Field, L. Frassinetti, A. A. Schekochihin, J. Contributors, and the EUROfusion Tokamak Exploitation Team, "Reconstructions of electron-temperature profiles from EUROfusion Pedestal Database using turbulence models and machine learning," (2025), arXiv:2504.17486 [physics.plasm-ph].
- <sup>27</sup>B. Efron and R. Tibshirani, Statistical Science **1**, 54 (1986).
- <sup>28</sup>P. Rodriguez-Fernandez, N. Howard, and J. Candy, Nuclear Fusion 62, 076036 (2022).
- <sup>29</sup> A. Ho, L. Zanisi, B. de Leeuw, V. Galvan, P. Rodriguez-Fernandez, and N. T. Howard, Physics of Plasmas 32, 093903 (2025).
- <sup>30</sup>D. L. C. Agapito Fernando, A. ñón Navarro, D. Carralero, A. Alonso, A. Di Siena, J. L. Velasco, F. Wilms, G. Merlo, F. Jenko, S. Bozhenkov,

- E. Pasch, G. Fuchert, K. J. Brunner, J. Knauer, A. Langenberg, N. Pablant, T. Gonda, O. Ford, L. Vanó, T. Windisch, T. Estrada, E. Maragkoudakis, and the Wendelstein 7-X Team, Physics of Plasmas **32**, 073904 (2025).
- <sup>31</sup>M. Landreman, J. Y. Choi, C. Alves, P. Balaprakash, M. Churchill, R. Conlin, and G. Roberg-Clark, Journal of Plasma Physics 91, E120 (2025).
- <sup>32</sup>F. Jenko, W. Dorland, and G. W. Hammett, Physics of Plasmas 8, 4096 (2001).
- <sup>33</sup>J. L. Velasco, I. Calvo, F. Parra, and J. M. García-Regaña, Journal of Computational Physics 418, 109512 (2020).
- <sup>34</sup>J. L. Velasco, I. Calvo, F. Parra, V. d'Herbemont, H. Smith, D. Carralero, T. Estrada, and the Wendelstein 7-X Team, Nuclear Fusion 61, 116013 (2021).
- <sup>35</sup>A. Shestakov, R. Cohen, J. Crotinger, L. Lodestro, A. Tarditi, and X. Xu, Journal of Computational Physics 185, 399 (2003).
- <sup>36</sup>J. Parker, L. LoDestro, D. Told, G. Merlo, L. Ricketson, A. Campos, F. Jenko, and J. Hittinger, Nuclear Fusion 58, 054004 (2018).
- <sup>37</sup>D. Carralero, T. Estrada, E. Maragkoudakis, T. Windisch, A. Alonso, M. Beurskens, S. Bozhenkov, I. Calvo, H. Damm, O. Ford, G. Fuchert, J. M. García-Regaña, N. Pablant, E. Sánchez, E. Pasch, J. L. Velasco, and the Wendelstein 7-X Team, Nuclear Fusion 61, 096015 (2021).
- <sup>38</sup>D. Carralero, T. Estrada, E. Maragkoudakis, T. Windisch, A. Alonso, J. L. Velasco, O. Ford, M. Jakubowski, S. Lazerson, M. Beurskens, S. Bozhenkov, I. Calvo, H. Damm, G. Fuchert, J. M. García-Regaña, U. Höfel, N. Marushchenko, N. Pablant, E. Sánchez, H. Smith, E. Pasch, T. Stange, and the Wendelstein 7-X Team, Plasma Physics and Controlled Fusion 64, 044006 (2022).